Dipole Engineering of Two-Dimensional van der Waals Heterostructures for Enhanced Power-Conversion Efficiency: The Case of Janus Ga_2SeTe/InS

Kun Liang,[1] Tao Huang,[1] Ke Yang,[1] Yuan Si,[1] Hong-Yu Wu,[1] Ji-Chun Lian,[1] Wei-Qing Huang,[1,*] Wang-Yu Hu,[2] and Gui-Fang Huang[1,†]

[1] *Department of Applied Physics, School of Physics and Electronics, Hunan University, Changsha 410082, China*
[2] *School of Materials Science and Engineering, Hunan University, Changsha 410082, China*

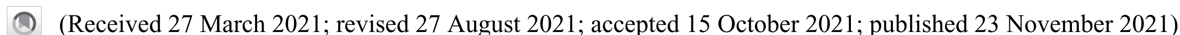
(Received 27 March 2021; revised 27 August 2021; accepted 15 October 2021; published 23 November 2021)

Highly efficient separation of tightly bound excitons (photoinduced electron-hole pairs) at an interface is crucial for high-performance two-dimensional (2D) heterostructure solar cells. Here we propose and demonstrate a strategy—dipole engineering—to effectively separate excitons at a 2D interface, which could evidently enhance power-conversion efficiency (PCE) via Heyd-Scuseria-Ernzerhof density functional calculations. The proposed dipole engineering is based on the synergetic effect of the intrinsic dipole in 2D Janus materials and interface dipole caused by charge transfer at the interface of 2D van der Waals heterostructures, in stark contrast to those strategies previously used, such as applying a strain or electric field. Taking the Janus Ga_2SeTe/InS heterostructure as an example, we demonstrate that the PCE can be promoted to a peak value of 23.2% when the intrinsic and interface dipoles are in the same direction, when accompanied by an appropriate applied compression strain. In addition, the Janus heterostructure possesses suitable band-edge positions of redox reaction potentials for full water splitting. Our work may herald an intrinsic yet effective way for enhancing the performance of optoelectronic devices, in contrast to the conventional external stimuli strategy.

DOI: 10.1103/PhysRevApplied.16.054043

I. INTRODUCTION

The direct conversion of solar energy to electricity by photovoltaic solar cells, or hydrogen energy via photocatalysis, has been emerging as a leading contender for next-generation green power production, which is the relentless pursuit of alternative fuels to solve the energy shortage and environmental pollution [1–3]. An efficient solar cell must absorb over a broad spectral range, from visible to near-infrared wavelengths (350–750 nm), and convert the incident light effectively into charges [4]. To achieve substantial energy-conversion efficiencies, these charges (generally, photogenerated electron-hole pairs) need to be dissociated into free charge carriers with a high yield, which are expected to be collected at a high voltage with a suitable current [5]. In this regard, heterojunctions with interfaces at which excitons can be dissociated are suitable structures for solar cells. For heterojunction solar cells, the power-conversion efficiency (PCE) is primarily determined by the short-circuit current density (J_{SC}) and open-circuit voltage (V_{OC}), which are closely related to the near-gap electronic structure [6–8].

Two-dimensional (2D) semiconductor-based heterojunction solar cells have recently become a focus of interest [9–11]. Particularly, those heterostructures with staggered type-II band alignment, which is conducive to the spatial separation of photogenerated electron-hole pairs, display greatly enhanced PCE. For instance, 2D graphene/GaAs [12] and GeS/GaSe [13] heterojunction solar cells have achieved PCEs of up to 16.2% and 16.8%, respectively. Interfacial recombination and carrier-extraction losses at the interface between donor layer and acceptor layer are the two main obstacles to further improving the PCE. To date, three strategies that all concentrate on tuning interface properties have been proposed to address these issues. The first one is strain engineering that prevails as a key way to tune the near-gap electronic structure of the heterojunction by mechanical strain, thus mitigating interfacial recombination to promote the photovoltaic performance. For instance, applying a tensile strain of 5% can enhance the PCE from 11.96% to 17.24% for the BP/SnSe van der Waals (vdW) heterostructure [14], while a tensile strain of only 2% will elevate the PCE value up to 19.9% in the MoSSe/blue phosphorene vdW heterostructure [15]. The second way to reduce interfacial recombination is to apply an external electric field across the interface to accelerate charge separation, thus attaining a higher yield. A prominent example is

*wqhuang@hnu.edu.cn
†gfhuang@hnu.edu.cn

 © 2021 American Physical Society

the SbI_3/BiI_3 heterostructure solar cell: its PCE could be raised from 14.42% up to 21.63% under a positive electric field [16]. The third strategy is to insert a high work function interlayer between donor and acceptor layers, obtaining field-effect passivation to effectively suppress the interfacial recombination and improve interfacial charge transfer [17]. The nature of these three strategies is that external stimuli, such as strain, electric field, or additional materials, are required to improve the solar cell's performance. Naturally, one intriguing question arises about whether the performance of heterostructure solar cells could be enhanced by utilizing only the intrinsic properties of individual components, rather than external stimuli.

Here we firstly propose dipole engineering as a strategy to tune the performance of heterostructure solar cells based on Heyd-Scuseria-Ernzerhof (HSE06) density functional [18,19] calculations. The core of this strategy is to make use of the synergetic effect of the intrinsic dipole in 2D Janus materials and the interfacial dipole caused by charge transfer at the interface of 2D vdW heterostructures; this strategy is totally different from those previously used, such as applying a strain or electric field. To demonstrate the effect of dipole engineering on PCE, a Janus Ga_2SeTe/InS heterostructure is chosen as an example. The choice of Janus Ga_2SeTe [one of the Janus group-III dichalcogenides ($M2XY$, $M = $ Ga, In; X, $Y = $ S, Se, Te), a family of layered materials with honeycomb structures] and InS monolayers is motivated by their excellent photoelectronic properties, such as wide optical absorption range and high absorption coefficient. For instance, Janus Ga_2SeTe, as a direct semiconductor with a band gap of around 1.2 eV, possesses a strong absorption coefficient (up to 10^5 cm^{-1}) [20,21]. The InS monolayer is a promising material to fabricate the stacking layered vdW heterostructures with staggered type-II band alignment for highly efficient solar cells (such as the InS/InSe heterostructure with a PCE of 13.7%) [22]. Most importantly, a large intrinsic vertical dipole (approximately 0.10 D, Fig. 1) exists in the Janus Ga_2SeTe monolayer due to its structural symmetry breaking, which could facilitate spatial separation of photogenerated carriers [23,24].

Our results show that for the case of certain configurations of a Janus Ga_2SeTe/InS heterostructure with staggered type-II band alignment, the PCE can be raised to a peak value of 23.2% when the intrinsic and interfacial dipoles are in the same direction, when accompanied by an

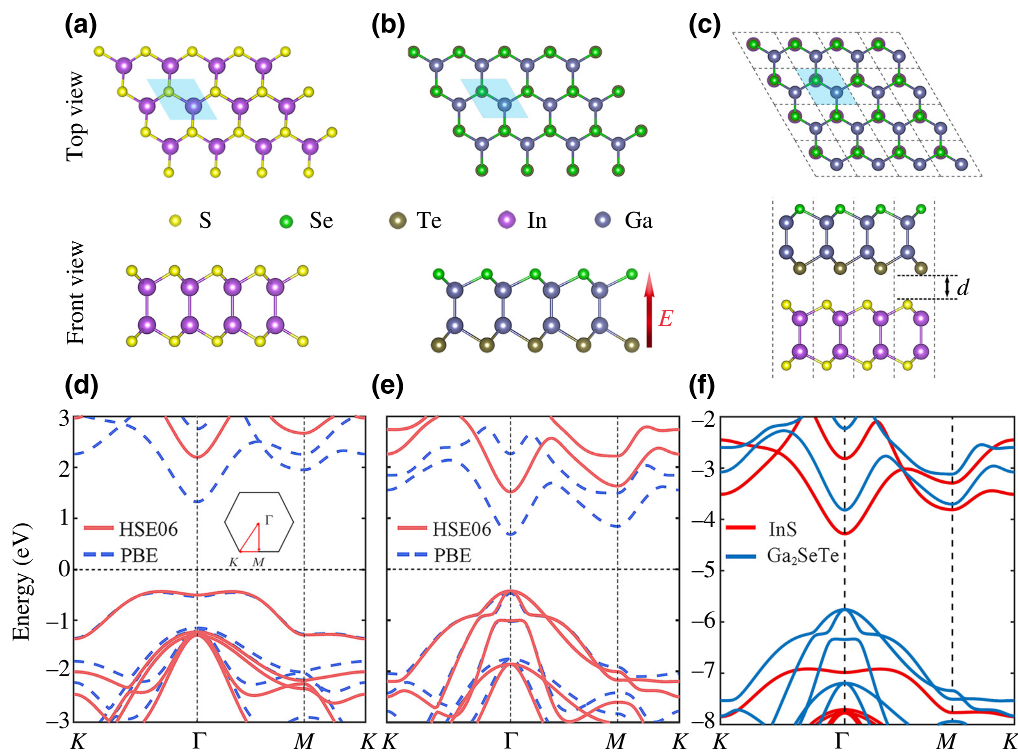

FIG. 1. Top and front views of the optimized geometric atomic structures of (a) InS, (b) Janus Ga_2SeTe monolayers, and (c) Janus Ga_2SeTe/InS heterostructure. The blue shaded area represents the unit cells of both monolayers and heterostructure. The red arrow indicates the intrinsic dipole direction in Janus Ga_2SeTe. The light yellow, green, brown, violet, and dark blue balls represent S, Se, Te, In, and Ga, respectively. (d) and (e) Schematics of the band structures of monolayer InS and Janus Ga_2SeTe calculated by PBE (blue dashed line) and HSE06 (red full line) functionals. The Fermi level (black dashed line) is shifted to zero. (f) The overlap band structures of isolated InS and Ga_2SeTe monolayers calculated by the HSE06 functional. Here, the vacuum level is set to zero.

applied compression strain of 4%. In addition, this Janus heterostructure possesses suitable band-edge positions of redox reaction potentials for full water splitting. This work demonstrates that dipole engineering is an effective strategy by using intrinsic properties, rather than conventional external stimuli methods, to tune the optoelectronic performance of Janus vdW nanodevices.

II. COMPUTATIONAL METHODS

First-principles calculations have been carried out using the Vienna *Ab initio* Simulation Package (VASP) based on density functional theory (DFT) [25–27]. The generalized gradient approximation in the form of Perdew-Burke-Ernzerhof (PBE) is formulated by the exchange and correlation potentials for the calculations of geometries and band structures [28]. This takes the approach of Grimme (DFT-D3) with the PBE functional for describing the long-range interaction using the dispersion potential in the vdW heterostructures [29–31]. For both accuracy and efficiency, the Brillouin zone is sampled on a Γ-centered k-mesh of $11 \times 11 \times 1$ in structure optimization of the Janus Ga_2SeTe and InS monolayers, and $9 \times 9 \times 1$ for formed heterostructures, respectively [32]. Under the periodic boundary condition, the vacuum depth in the z direction is set to 30 Å to avoid the artificial interaction between two adjacent layers. The cutoff energy of the plane-wave basis set is chosen to be 450 eV, and the total convergent tolerance in energy and the forces on each atom converge are set to less than 10^{-6} eV and 0.01 eV $Å^{-1}$. Given that the PBE functional probably underestimates the band gap, the HSE06 hybrid functionals are adopted for a more accurate property determination. In addition, the crystal structures and charge distributions are visualized through VESTA. Note that the dipole correction has an ignorable impact on the electronic structures of the monolayers and heterostructures investigated here, thus we do not consider the dipole correction in the following calculations.

For 2D monolayers and their heterostructures, the optical absorption spectra are rather essential to explore the intrinsic properties for applications in optoelectronic devices. To quantitatively understand the absorption spectra, the optical absorption coefficient $\alpha(\omega)$ is calculated using the following equation:

$$\alpha(\omega) = \sqrt{2}\omega\left[\sqrt{\varepsilon_1^2(\omega) + \varepsilon_2^2(\omega)} - \varepsilon_1(\omega)\right]^{1/2}$$

where $\varepsilon_1(\omega)$ and $\varepsilon_2(\omega)$ are the real and imaginary parts of the complex dielectric function, respectively, and the real part of the dielectric function could be obtained from $\varepsilon_2(\omega)$ by the Kramers-Kronig transformation. $\varepsilon_2(\omega)$ is given by the expression

$$\varepsilon_2(\omega) = \frac{4\pi^2 e^2}{\Omega} \lim_{q\to 0} \frac{1}{q^2} \sum_{c,v,\vec{k}} 2w_k \delta(\varepsilon_{ck} - \varepsilon_{vk} - \omega) \times \langle \mu_{ck+e_\alpha} | u_{vk}\rangle \langle \mu_{ck+e_\beta} | \mu_{vk}^*\rangle$$

where Ω, c, and v represent the unit-cell volume, the states of valence bands, and conduction bands, respectively. The indices ω and u correspond to the photon frequency and the vector defining the polarization of the incident electric field.

The PCE is another critical basis to explore the ability of utilizing solar energy, which is defined as follows [33]:

$$\eta = \frac{J_{\text{SC}} V_{\text{OC}} \beta_{\text{FF}}}{P_{\text{solar}}} = \frac{0.65(E_g^d - \Delta E_c - 0.3) \int_{E_g}^{\infty} (P(\hbar\omega)/\hbar\omega) d(\hbar\omega)}{\int_0^{\infty} P(\hbar\omega)\hbar\omega}$$

where the band-fill factor β_{FF} is the empirical value derived by Shockley-Queisser, and is assumed to be 0.65; the maximum open-circuit voltage is expressed by $(E_g^d - \Delta E_c - 0.3)$; E_g^d and ΔE_c represent the band gap of the donor layer and the conduction-band offset (CBO) of the heterostructure, respectively; $P(\hbar\omega)$ represents the AM1.5 solar energy flux at the photon energy, which is defined as $\hbar\omega$. The integrals in the numerator and denominator represent the short-circuit current and the sum of AM1.5 incident solar irradiation, respectively. E_g^d is regarded as the lower limit of integration of the term $\int_{E_g}^{\infty} [P(\hbar\omega)/\hbar\omega] d(\hbar\omega)$, where the electrons would be excited into a higher level after absorbing photon energy over E_g^d. In addition, it is found that the PCE is strongly correlated to the CBO between the donor and acceptor layers in heterostructures.

III. RESULTS AND DISCUSSION

Initially, we investigate the geometric and electronic properties of individual layers before fabricating 2D heterostructures of Janus Ga_2SeTe and InS monolayers. Both InS and Janus Ga_2SeTe monolayers composed of four atomic layers are stacked in the sequence of $X/M/M/X(Y)$ ($M =$ Ga, In; X, $Y =$ S, Se Te), which display high degrees of mirror symmetry and asymmetry characteristics respectively, as shown in Figs. 1(a) and 1(b). The optimized lattice constants of InS and Janus Ga_2SeTe monolayers are 3.91 and 3.94 Å, respectively, suggesting the likelihood of epitaxial stacking, especially in few-layer systems. The calculated bond lengths l are listed in Table I, in which all show good agreement with previous reports [34,35], indicating the reliability of the following calculated results. In Fig. 1(b), the different surface chalcogen atoms of the

TABLE I. Calculated lattice parameter a_0 (Å), bond length l (Å), work function WF (eV), band gap Eg (eV) of each monolayer.

Monolayer	a_0 (Å)	$l_{\text{In-In}}$ (Å)	$l_{\text{In-S}}$ (Å)	$l_{\text{Ga-Ga}}$ (Å)	$l_{\text{Ga-Se}}$ (Å)	$l_{\text{Ga-Te}}$ (Å)	W_F (eV)	E_g (eV) PBE	E_g (eV) HSE06
InS	3.91	2.798	2.556	–	–	–	6.48	1.74	2.63
Ga_2SeTe	3.94	–	–	2.496	2.546	2.664	5.34	1.20	1.96

Janus Ga_2SeTe monolayer result in different coordination environments of Ga atoms in the middle layer, where the centrosymmetry of the 2D plane is broken, and gives rise to an intrinsic dipole, leading to an internal electric field pointing from the Te atom plane to the Se atom plane (shown by the red arrow). The dipole moment per unit cell of the Janus Ga_2SeTe monolayer is calculated to be about 0.10 D (left panel of Fig. 2), which is favorable to the separation of photogenerated carriers. The band structures of Janus Ga_2SeTe and InS monolayers are theoretically calculated using the PBE and HSE06 methods, and the chosen high-symmetry points and integral paths in the first Brillouin zone are described in the inset of Fig. 1(d). It is found that both monolayers have a semiconductor nature with hexagonal structure. In detail, the InS monolayer shows an indirect band gap, in which the conduction-band maximum (CBM) located at the high symmetric point Γ, while the valence-band minimum (VBM) presents an interesting Mexican-hat shape at the high symmetric point on the Γ-K and Γ-M paths. In contrast, the Janus Ga_2SeTe monolayer has a direct semiconductor characteristic, in which both CBM and VBM locate at the Γ point. The gap values of Janus Ga_2SeTe and InS monolayers are calculated to be about 1.74 eV (2.63 eV) and 1.20 eV (1.96 eV) by the PBE (HSE06) functional; these values are consistent with the previous theoretical calculations [36,37].

Owing to the unique intrinsic structure of 2D Janus materials, the interfacial configuration of heterostructures is strongly correlated with the terminated surface and atom alignment of individual layers. Here, four different stacking configurations of Janus Ga_2SeTe/InS vdW heterostructures are designed according to the alternating positions of Se (Te) atomic layers on opposite surfaces of the Janus monolayer, which are denoted as *AA*1, *AA*2, *AB*1, and *AB*2, respectively (depicted in Fig. 2). The stacking sequence of atoms in model I (II) is the S atomic layer at the bottom of InS corresponds to the Se (Te) atomic layer at the top of Janus monolayer. In *AA*1 and *AA*2 stackings, atoms of the InS monolayer are fixed to the position corresponding to the Ga atoms of the Janus Ga_2SeTe monolayer. From the top view, two monolayers directly overlap in space, and all chalcogen and transition-metal atoms are aligned. In contrast, the bottom monolayers of *AB*1 and *AB*2 stackings are rotated by 180°along with the

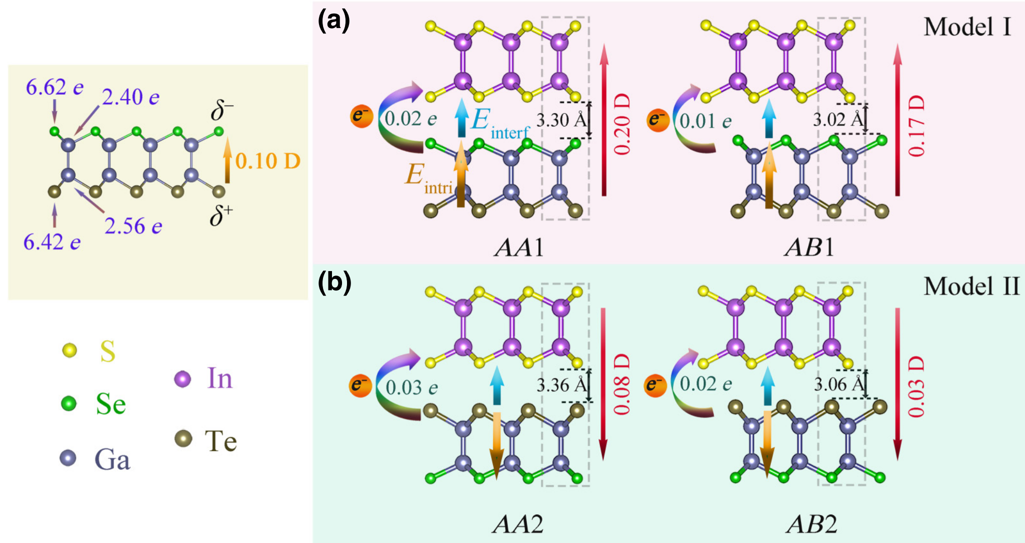

FIG. 2. (Left panel) Illustration of the intrinsic out-of-plane dipole (approximately 0.01 D, orange arrows), from Ga atom plane to Se atom plane, in polar Janus Ga_2SeTe monolayer, owing to its broken mirror symmetry to the basal plane. The numbers show the calculated Bader charges. (a) and (b) Schematics of four stacking configurations (*AA*1, *AA*2, *AB*1, and *AB*2), charge transfer (colored curved arrows), interface dipole (blue arrows), intrinsic dipole (brown arrows) interfacial distance (black arrows), and net dipole (red arrows) of the Janus Ga_2SeTe/InS vdW heterostructure.

TABLE II. Calculated lattice parameter d (Å), binding energy E_b (eV/cell), net dipole moment d_μ (D), work function W_F (eV), conduction-band offset (CBO), donor band gap (E_d), band gap E_g (eV) of all the optimized heterostructures, and their Bader charge.

Stacking	d (Å)	E_b (eV/cell)	d_μ (D)	W_F (eV)	CBO (eV)	E_d (eV)	E_g (eV)		Bader charge (e)	
							PBE	HSE06	InS	Ga_2SeTe
*AA*1	3.966	−0.08	0.20	5.12	0.41	1.94	0.79	1.53	0.02	−0.02
*AB*1	3.927	−0.217	0.17	4.96	0.42	1.91	0.72	1.49	0.01	−0.01
*AA*2	3.977	−0.07	0.08	5.22	0.89	2.16	0.52	1.26	0.03	−0.03
*AB*2	3.932	−0.219	0.03	5.10	0.68	2.10	0.64	1.42	0.02	−0.02

z axis relative to the InS monolayer, leading to the In atoms of the InS monolayer having a direct correspondence with the chalcogen atoms of Janus monolayer. To compare the relative stability of these configurations, their formation energies (E_f) are calculated according to the equation: $E_f = E_{\text{comb}} – E_{J-MX} – E_{\text{InS}}$, where E_{comb}, E_{J-MX}, and E_{InS} represent the calculated total energy of the relaxed heterostructures, isolated Janus Ga_2SeTe, and InS monolayer, respectively. On the basis of the definition given previously, the negative E_f indicates that the heterostructure is stable. The lower E_f forces these heterostructures to approach the lower-energy state and therefore a more stable configuration, suggesting that they can be synthesized in experiments more easily. Table II shows that the interface binding energies of the *AB* stackings are about -0.22 eV Å^{-2}, smaller than those (approximately 0.08 eV Å^{-2}) of *AA* stackings, demonstrating that the *AB* layer stacking is more energetically favorable than the *AA* stacking in both configurations, owing to the effect of atomic steric hindrance. This is also consistent with their smaller interface distance.

The most striking feature in Fig. 2 is the significant difference in the net dipoles in these configurations. Because the electronegativity of the S atom is larger than those of Se and Ga atoms, the electrons are always transferred from the Se or Ga atom to the S atom at the interfaces of the four configurations [Figs. 2(a)–2(d)]. The number of electrons transferred depends on the electronegativity difference and configuration. For instance, about 0.03 e (per unit) is transferred from the Janus Ga_2SeTe layer to the InS layer due to the bigger electronegativity difference between the S and Ga atoms in the *AA*2 stacking. It is emphasized especially that electron transfer across the interface creates an interface dipole (with related field, E_{interf}) that cannot be neglected in these heterostructures. The total net dipole in these stacking configurations is determined by the orientations of the interface dipole and intrinsic dipole of the Janus Ga_2SeTe layer; thus, it is possible to trigger dipole engineering. In the four stackings, the configurations with Se atoms facing S atoms (i.e., *AA*1 and *AB*1) have a larger net dipole because the orientations of the interface and intrinsic dipoles are the same [Fig. 2(a)]. As a consequence, the *AA*1 and *AB*2 stackings have biggest and smallest net dipoles (0.20 and 0.03 D), respectively. The different net dipoles would affect the electronic structures of the Janus Ga_2SeTe/InS vdW heterostructures.

We next focus on the electronic structures of Janus Ga_2SeTe/InS vdW heterostructures. The projected band structures of these heterostructures with different configurations are investigated using the HSE06 functional, and the schematic diagrams are presented in Fig. 3. It can be found that the intrinsic semiconductor characteristic appears in diverse band alignments of heterostructures. Among them, the *AA*1 and *AA*2 stackings exhibit an indirect band structure with type-V band alignment [38], where the CBM lies at the Γ point while the VBM is located on the Γ-*K* path, and the shape of the VB keeps the Mexican-hat-like pristine InS monolayer. In contrast, a type-II staggered band alignment appears in the *AB*1 and *AB*2 stackings, which display a direct band gap and both CBM and VBM are located at the Γ point. Furthermore, the calculated partial charge density of heterostructures demonstrates the contribution of isolated monolayers, and the main contributions to the CBMs of the *AB*1 and *AB*2 configurations are from the InS monolayer, while the VBMs result from the Ga_2SeTe layer (middle in Fig. 3), indicating both heterostructures possess a staggered type-II band alignment. To understand the effect of the dipole on the electronic properties in the heterostructure, we overlap the individual band structures of isolated monolayers with the same hexagonal cell and highly consistent lattice constant in one figure, presented in Fig. 1(f). For all stacking configurations, the projected band structure produces only a slight change compared with those before stacking, which is mainly caused by the energy differences of the orbitals near the bottom of the CB or the top of the VB of the two individual monolayers relative to the vacuum level. Electron transfer occurs between two adjacent monolayers, resulting in a slight movement of band edges. The band alignment near the Fermi level of all heterostructures is close to the overlap band structure of individual monolayers, which further verifies that two monolayers are connected by vdW forces rather than being covalent. Hence, the type-II band alignment appears in *AB*1 and *AB*2 stackings, where the positions of both the CB and VB of individual monolayers in their heterostructures are higher

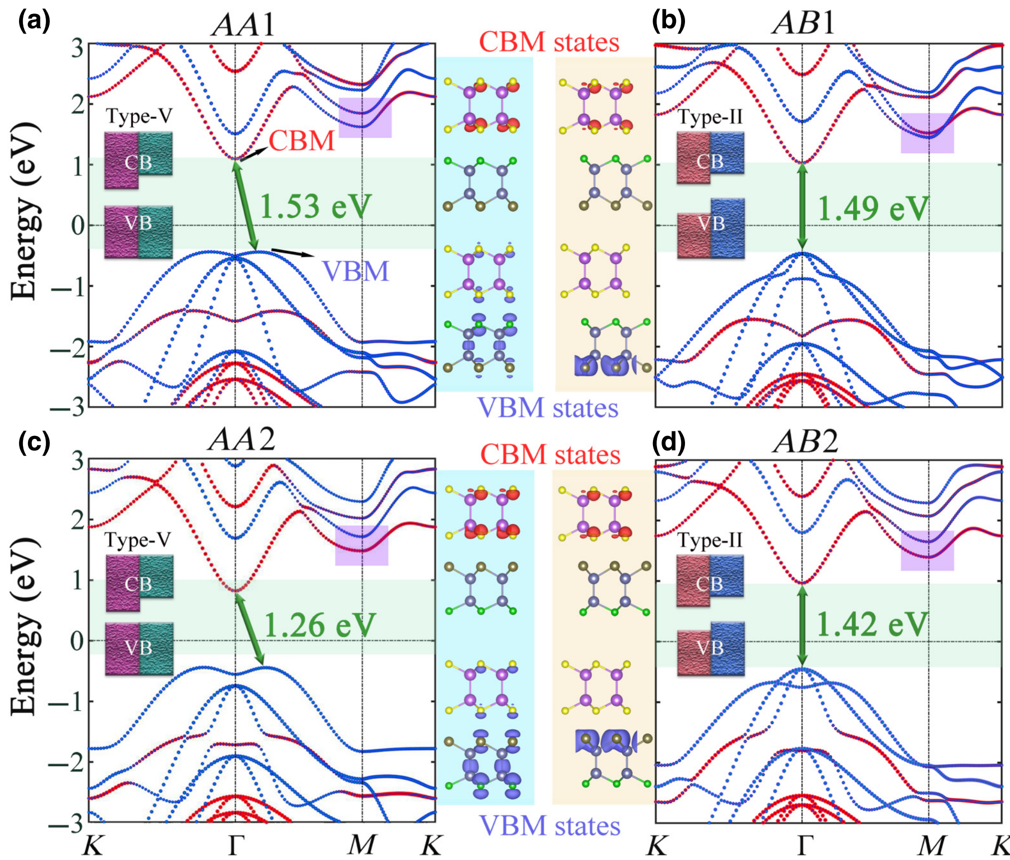

FIG. 3. Effects of interlayer interaction on the electronic structures of the Janus Ga_2SeTe/InS vdW heterostructure. (a)–(d) The projected band structures of the heterostructure with four stacking configurations. The red and blue lines represent contributions of the InS and Janus Ga_2SeTe monolayers, respectively. The numbers show the calculated band gaps (green arrows). The Fermi level is set to 0 eV (black dashed line). Insets: Schematic diagrams of corresponding band alignments. (Middle panel) Illustration of the partial charge densities for corresponding heterostructures. The red and blue regions represent contributions of the InS and Janus Ga_2SeTe monolayers, respectively. The isovalue is set to $6.5 \times 10^{-4}\, e\, \text{Å}^{-3}$.

(or lower) than their counterparts in the other, forming a smaller effective band gap (Table II), which is conducive to the separation of the excited electron-hole pairs between adjacent monolayers. These results suggest that the dipole in the heterostructure plays a significant role in band alignments.

To gain more detail of the contribution of isolated monolayers in Janus Ga_2SeTe/InS heterostructures, the partial density of states (PDOS) is calculated and illustrated in Fig. 4. On the whole, the CBM of the heterostructure is mainly contributed by the InS monolayer, while the VBM shows completely different behavior. In *AA*1 and *AA*2 configurations, the occupation of charge density at the VBM comes from two isolated monolayers, indicating the band offset of the valence bands is zero, revealing that an unconventional type-V band alignment appears in the heterostructures. In contrast, the charge density occupation in the VBM of the *AB*1 and *AB*2 configurations is only contributed by Se and Ga atoms of the Janus Ga_2SeTe layer, resulting in a staggered type-II band alignment.

To better characterize the interfaces with different configurations, the states of redistribution can be visualized by the three-dimensional (3D) charge density difference, defined as $\Delta\rho = \rho_H - \rho_{J-MX} - \rho_{\text{InS}}$ (as an explicit visualization method), where ρ_{H}, ρ_{J-MX}, and ρ_{InS} represent the charge densities of the heterostructures, isolated Janus Ga_2SeTe, and InS monolayers, respectively. Figures 5(a) and 5(c) show the calculated 3D charge density differences of *AB*1 and *AB*2 stackings with an isovalue of $2.0 \times 10^{-4}\, e\, \text{Å}^{-3}$, where the orange and blue regions represent the charge accumulation and depletion at the interface, respectively. Furthermore, the planar charge density difference is averaged as a function of position along the *z* direction and plotted in parallel to the heterostructure, where the oscillations present the charge transfer status in space. It is clear that the charge transfer is mainly distributed by adjacent atomic layers, and the regions of electron and hole accumulation are close to the InS and Janus Ga_2SeTe layers. Owing to the effects of the intrinsic dipole of the Janus Ga_2SeTe monolayer and the interface dipole, the electrons and holes are separated on the Se and Te atom plane of the Janus Ga_2SeTe monolayer, while more holes are accumulated in the Te atom plane of the $SeGa_2Te$/InS heterostructure, which can effectively promote the transfer of charge from the Janus Ga_2SeTe to the InS monolayer. Owing to the difference in electronegativity and atomic radius of Se and Te atoms, the amount of charge transfer in *AB*2 stacking is much larger than in *AB*1 stacking, corresponding to the larger amplitude in oscillations between individual monolayers. Moreover, the quantitative analysis method based on the Bader charges shows that the quantity of charge transfer is about 0.01 and 0.02 per unit cell of the *AB*1 and *AB*2 stackings,

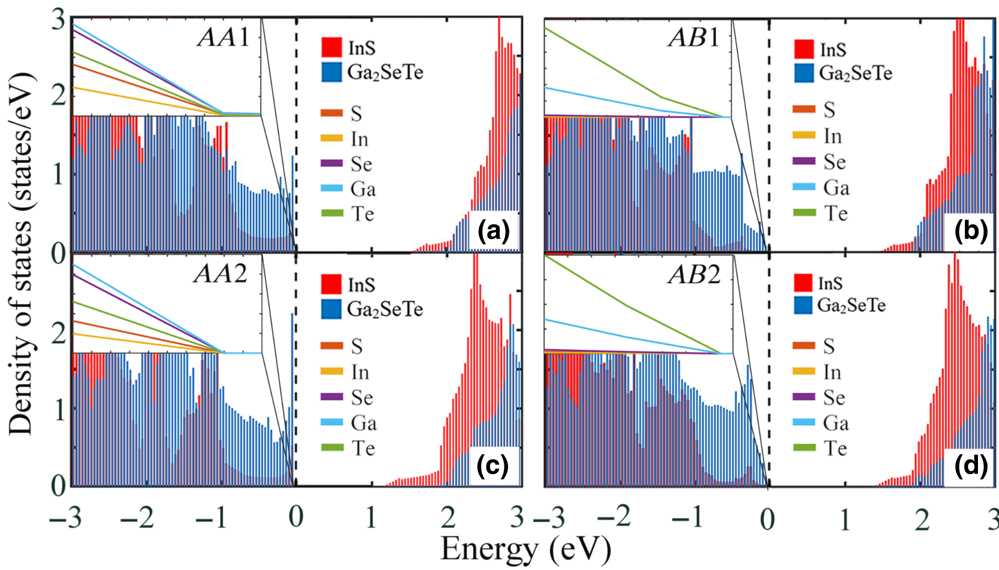

FIG. 4. (a)–(d) The calculated total density of states (TDOS) and partial density of states (PDOS) (upper left insets) of the Janus Ga_2SeTe/InS vdW heterostructures with four stacking configurations.

respectively, which are smaller than those of the *AA*1 and *AA*2 stackings, as presented in Table II.

The electrostatic potential of heterostructures may be changed due to the charge redistribution at the interface. Figures 5(b) and 5(d) present the corresponding plane-averaged electrostatic potential as a position function with $z =$ constant along the vacuum layer for the type-II Janus Ga_2SeTe/InS heterostructures. The potential drop (ΔV) across the interface is formed, leading to an effective built-in electric field between individual layers. The work functions of Ga_2SeTe, InS, and their heterostructures are calculated and are marked on the profiles of the planar-averaged electrostatic potential, as shown in Figs. 5(b) and 5(d). The calculated work functions are associated with the difference of electrostatic potential in the vacuum region relative to the Fermi level ($V_{\text{vacuum}} - E_F$). Comparing the energy levels of Janus Ga_2SeTe and InS layers, the former is significantly higher than the latter, and the position of formed heterostructures is somewhere between the two individual layers, indicating the transfer direction is from the Janus Ga_2SeTe (donor) to InS (acceptor) monolayer in the charge transfer process. Furthermore, the migration of photogenerated carriers is greatly influenced by the built-in electric field at the interface, in which the potential well is conducive to the separation of the photogenerated carriers and effectively restrains the recombination of photogenerated electron-hole pairs in the heterostructures.

To more clearly illuminate the migration of carriers at the interface, we draw the migration schematic of photogenerated electron-hole pairs in Janus Ga_2SeTe/InS heterostructures. In Fig. 6, the photogenerated electrons flows from the VB of the InS layer to the CB of the Ga_2SeTe layer after gaining external photon energy under solar radiation. Meanwhile, the VB of the InS layer generates corresponding holes in the transport process, and these holes migrate to the Ga_2SeTe layer. Thus, a built-in electric field (E_{interf}) appears at the interface. Meanwhile, the calculated CBO and valence-band offset (VBO) of *AB*1 (*AB*2) stackings are 0.42 (1.10) eV and 0.68 (1.35) eV, respectively, as listed in Table II. These results indicate that the *AB*1 stacking can significantly lower the recombination rate of the photogenerated electron-hole pairs between isolated layers, and have potential applications in photoelectric devices.

For applications in photoelectric devices, optical absorption properties are key parameters, such as in developing photosensitive photodetectors and efficient solar cells. Figure 7(a) displays the absorption spectra of each layer and their type-II heterostructures. Although both monolayers can absorb visible light, their absorption is relatively low. Compared with isolated monolayers, the optical absorption of both type-II heterostructures is enhanced in the range from ultraviolet to visible light (approximately 300–750 nm), which mainly results from the narrow band gap of heterostructures after stacking layers. In particular, the Janus $TeGa_2Se/InS$ heterostructure (*AB*1 stacking) system shows greater solar absorption in the whole visible region, indicating enough photon energy can be utilized, and further develop optical applications. Therefore, Janus Ga_2SeTe/InS heterostructures may have great potential in solar light harvesting.

Considering the type-II band alignment and high absorption coefficient in the visible light region of Janus Ga_2SeTe/InS heterostructures, we investigate the PCE for exploiting these properties in highly efficient solar cell applications. Referring to the method of Scharber's work [6], the PCE of the heterostructure is rather crucial for evaluating the capacity of converting photon energy. The calculated PCE contour plots of the Janus Ga_2SeTe/InS heterostructures are displayed in Fig. 7(b), in which those

of GaSe/InS and GaTe/InS are also presented for comparison. According to the previous theoretical results, the PCE of the GaSe/InS and GaTe/InS heterostructures are about 4.85% and 8.20%, respectively [22]. The calculated PCEs of *AB*1 (Janus $TeGa_2Se$/InS) and *AB*2 (Janus $SeGa_2Te$/InS) stacking heterostructures are approximately 13.1% and 17.7%, indicating that the intrinsic dipole in the Janus layer can improve the solar cell performance. It should be pointed out that, in most cases, dipole correction for 2D Janus materials would affect the calculation results qualitatively [23]. Therefore, we also calculate the PCE including the dipole correction. The results show that the calculated PCE value of Janus $SeGa_2Te$/InS heterostructure has an ignorable variation when dipole correction is considered.

As is well known, the excitonic effect for most 2D materials (such as, transition-metal dichalcogenides) strongly affects the optical properties due to the weak screening effect and large excitonic binding energy; the latter is an important factor in photovoltaics as the formation of excitons influences the charge separation in solar cells. In order to investigate the excitonic effect on PCE, we also perform *GW* and Bethe-Salpeter equation (BSE) calculations. Figure 7(c) shows the *GW* band structure and density of states of *AB*1 stacking (Janus $TeGa_2Se$/InS). We find that the band dispersions, CBO, and VBO between Janus Ga_2SeTe and InS monolayers from the *GW* calculations are very similar to those from the HSE06 method, although the band gap increases (1.49 eV for HSE06 vs 1.78 eV for *GW*). The increased band gap is because the *GW* approach includes a more accurate electron-electron correlation effect compared with the HSE06 approach. To obtain better optical properties, we also perform BSE calculations based on the *GW* calculation. Although the quasiparticle band gap from *GW* is larger than that from HSE06, the excitonic effect (excitonic binding energy is 0.35 eV for the lowest exciton) reduces the optical absorption edge to 1.43 eV. One can see from Fig. 7(d) that the absorption calculated by the *GW*-BSE method is similar to that of the HSE06 approach. More interestingly, using the electronic structure and optical properties based on the *GW*-BSE calculations, the calculated PCE value is very close to that based on the HSE06 approach (16.5% from *GW*-BSE vs 17.7% from HSE06), as shown in Fig. 7(b). This indicates that the HSE06 approach used here is valid to investigate the solar cell performance of 2D heterostructures.

In general, strain engineering is considered to be a feasible strategy to adjust electronic and optical properties, especially the band alignment and PCE of heterostructures. Given the experimental feasibility, an in-plane biaxial strain (Fig. 8) varying from −6% to +6% (the positive and negative values represent the tensile and compressive strains, respectively) is applied to explore its effect on the electronic properties and PCE of the *AB* stacking based on the HSE06 functional. To gain more convenient and intuitive understanding, the schematic diagram of the heterostructure under strain engineering is displayed in Fig. 8(a). Here, the Janus Ga_2SeTe monolayer is taken as donor and the InS monolayer as acceptor. The band-edge position and band gap of the Janus Ga_2SeTe/InS heterojunction as a function of in-plain biaxial strains are presented in Figs. 8(b) and 8(c), in which the effective tunability of the band alignment and band gaps by strain engineering is clearly demonstrated. Obviously, there is a knee point positioned at 0% biaxial strain for both *AB*1 and *AB*2 stackings, demonstrating that their band gap decreases under biaxial strain. Moreover, the band gap in both stackings decreases monotonically with biaxial strain, although it decreases linearly with increasing tensile strain, while not under compressive strain. In fact, the variation of band gap in both stackings can be attributed to the movement of positions of the CBM and VBM under biaxial strain. For the *AB*1 stacking, the positions of CBM and VBM shift to lower energy from the maximum compressive strain to the maximum tensile strain (i.e., −6% to +6%), as

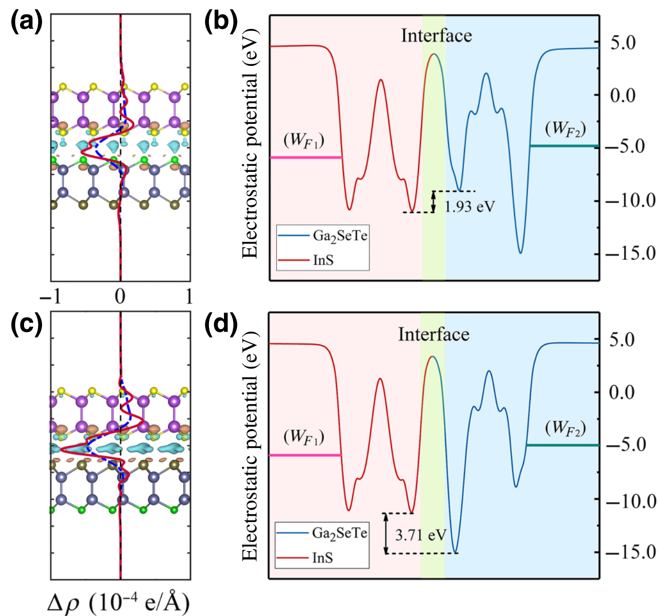

FIG. 5. The detail charge transfer and the planar averaged self-consistent electrostatic potential as a function of position in Janus Ga_2SeTe/InS vdW heterostructures along the *z* direction with (a) and (b) *AB*1, and (c) and (d) *AB*2 stacking configurations. (a) and (c) Illustration of charge accumulation (orange regions) and depletion (blue regions) at the interface, original data (red solid line) and position function (blue dashed line) of heterostructures. Three-dimensional charge density difference of heterostructures with the isovalue of 2.0×10^{-4} e Å^{-3}. (b) and (d) W_{F1} and W_{F2} represent the position of work functions for the InS (carmine line) and Janus Ga_2SeTe (dark green line) monolayer in the corresponding heterostructure. The numbers show the calculated potential drops of two monolayers at the interface (black double-arrow).

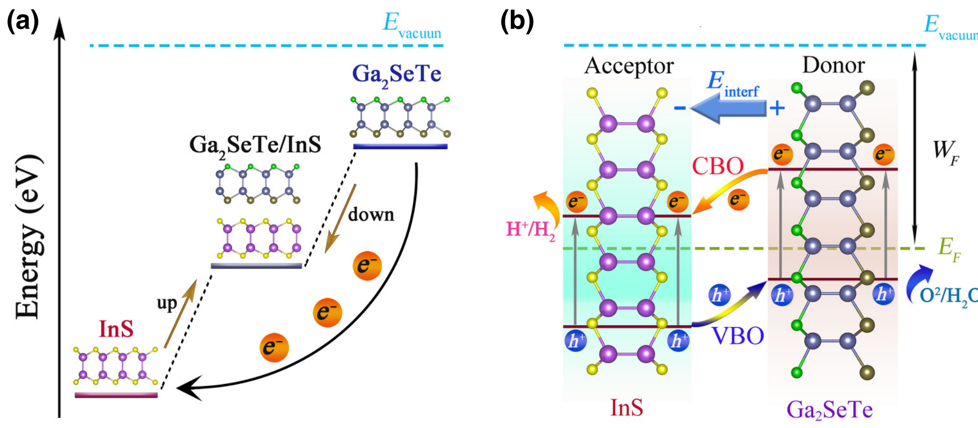

FIG. 6. (a) The flow directions of electrons and the shift of the Fermi level after forming the heterostructure. (b) Schematic of the migration of photogenerated carriers at the interface of *AB*1 stacking.

displayed in Fig. 8(b). However, the shifting magnitude of the CBM and VBM positions is not simultaneous, thus resulting in a volcanolike plot of band gap under biaxial strain. Similarly, a volcanolike plot of band gap under biaxial strain can be observed in the *AB*2 stacking, although the positions of the CBM and VBM shift to higher energies as the compressive strain decreases from −6% to −3% [Fig. 8(c)].

Biaxial strain changes the atomic structure of monolayers and their interface distance, thus inducing the dipole and CBO variations. We calculate the total dipoles, intrinsic and interfacial dipoles, and CBOs of *AB*1 and *AB*2 stacking configurations of the Janus Ga_2SeTe/InS vdW heterostructure with different biaxial strains. Figures 8(d) and 8(c) display that the CBOs increasing with different speeds in *AB*1 and *AB*2 stacking configurations, as the strain varies from the maximum compressive strain to the maximum tensile strain (i.e., −6% to +6%). Interestingly, both the intrinsic and the interfacial dipoles [the insets in Figs. 8(d) and 8(c)] in the *AB*1 and *AB*2 stackings are increased as the strain changes from −6% to +6%. As expected, the net dipole increases in the *AB*1 stacking as the strain changes from −6% to +6%, while it slowly increases in the *AB*2 stacking as the strain reduces from −6% to −4%, and then obviously decreases up to the maximum tensile strain (6%). This is due to the fact that the intrinsic and interface dipoles [Fig. 1(a)] are in the same direction in the *AB*1 stacking, while they are

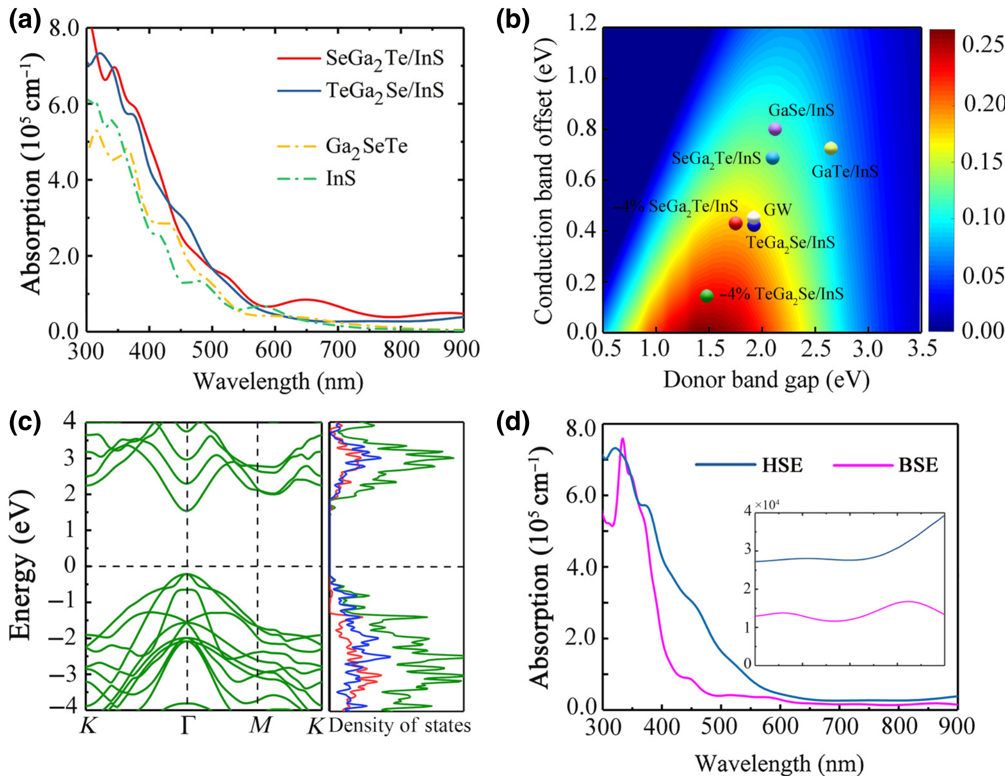

FIG. 7. (a) The optical absorption spectra of InS and Janus Ga_2SeTe monolayer and corresponding *AB*1 and *AB*2 stackings. (b) The calculated plots of PCE (%) as a function of donor band gap and CBO of heterostructures. (c) Band structures and projected PDOS of the *AB*1 stacking calculated by *GW*. The Fermi levels are shifted to zero. (d) The optical absorption spectra for *AB*1 stacking calculated by HSE06 and BSE. Inset: the local magnification of absorption spectra at 700–900 nm.

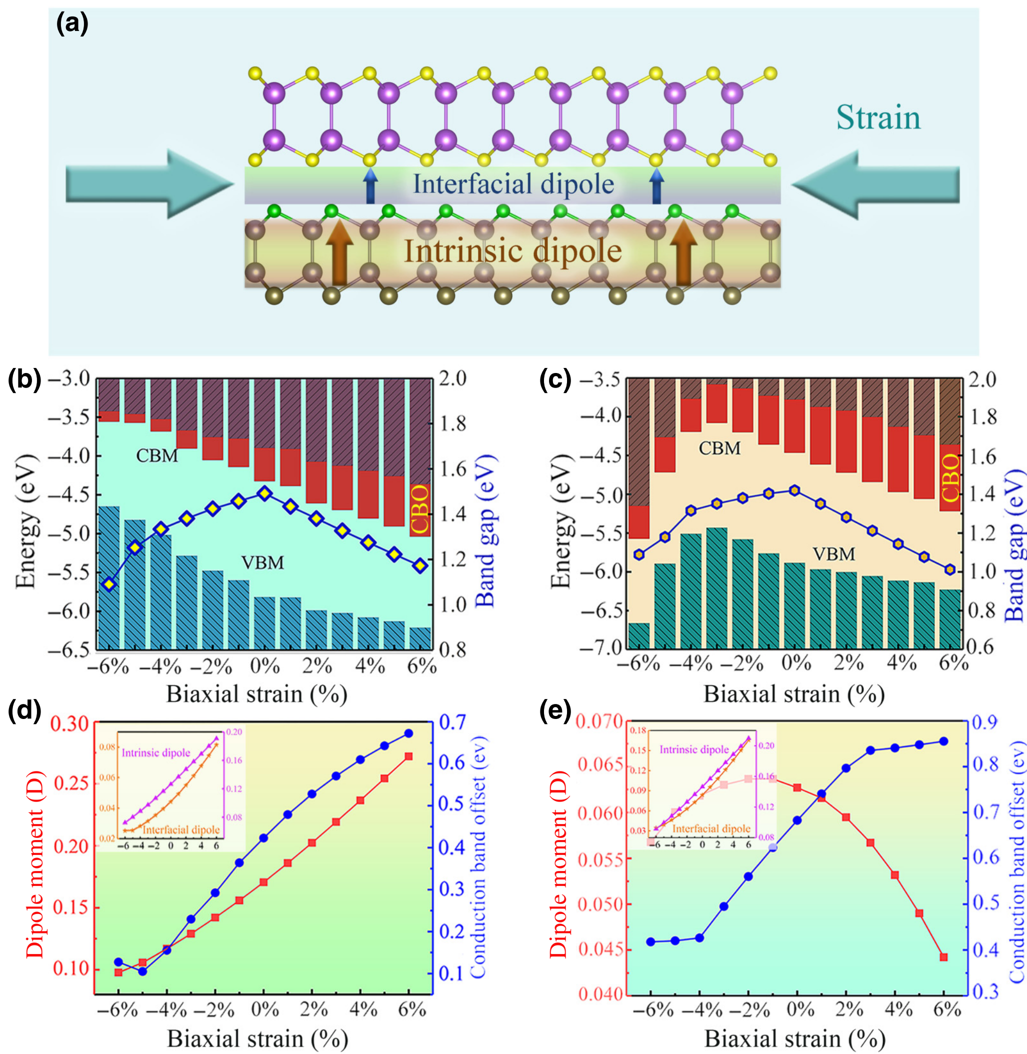

FIG. 8. (a) The schematic diagram of the $TeGa_2Se/InS$ vdW heterostructure under compressive strain. Evolution diagram of the band-edge position and the band gap of (b) *AB*1 and (c) *AB*2 stackings with different biaxial strains calculated by the HSE06 functional. Evolution diagrams of the total dipoles, intrinsic and interfacial dipoles (upper left insets), and CBOs of (d) *AB*1 and (e) *AB*2 stacking configurations of the Janus Ga_2SeTe/InS vdW heterostructure with different biaxial strains.

opposite in the *AB*2 stacking [Fig. 1(b)]. Following the PCE definition, we find the calculated PCEs of *AB*1 and *AB*2 stackings can be further elevated to 23.2% and 18.0% [Fig. 7(b)], respectively, by applying a 4% compressive strain, indicating the heterostructures can gain a superior capability of solar energy utilization. Hence, the biaxial strain modulation can be regarded as a feasible strategy to improve PCE values to above that of solution-processed organic tandem solar cells (12.7%) [39]. The PCEs of two stackings have a considerable competitive advantage compared with many previous reported homophylic photoelectric heterostructures, such as the N-doped GaX/SnS_2 (approximately 16%) [40], graphene/GaAs (18.5%) [41], and graphene/indium phosphide [42]. These results suggest that the Janus Ga_2SeTe/InS heterostructures can gain more superior photoelectric properties than those based on intrinsic monolayers, and be considered as desirable candidate nanomaterials for highly efficient solar cells.

For practical applications, electrostatic gating is another feasible method to investigate the external electric field modulation on the electronic properties of heterostructures. Taking the *AB*1 stacking for example, we consider the positive (negative) direction of electric field applied perpendicular to individual monolayers, which is set as pointing from the Janus Ga_2SeTe (InS) monolayer to InS (Janus Ga_2SeTe). The band gap as a function of external electric fields can be tuned effectively, as plotted in Fig. 9(a), depending on both the intensity and direction of the electric field. Here, the band gap will primarily rise to the maximum value of 1.65 eV through applying the positive electric field, and then monotonically fall to zero when the electric field strength increases to over 0.37 V/Å (0.25 V/Å for the negative direction). This demonstrates the transition from semiconductor to metal in the heterostructure, which results from the phenomena of charge tunneling and dielectric breakdown. Meanwhile, the heterostructure retains the characteristics of direct band gap when the electric field strength increases from −0.1 to 0.15 V/Å, which is conducive to light absorption. In addition, the evolution of

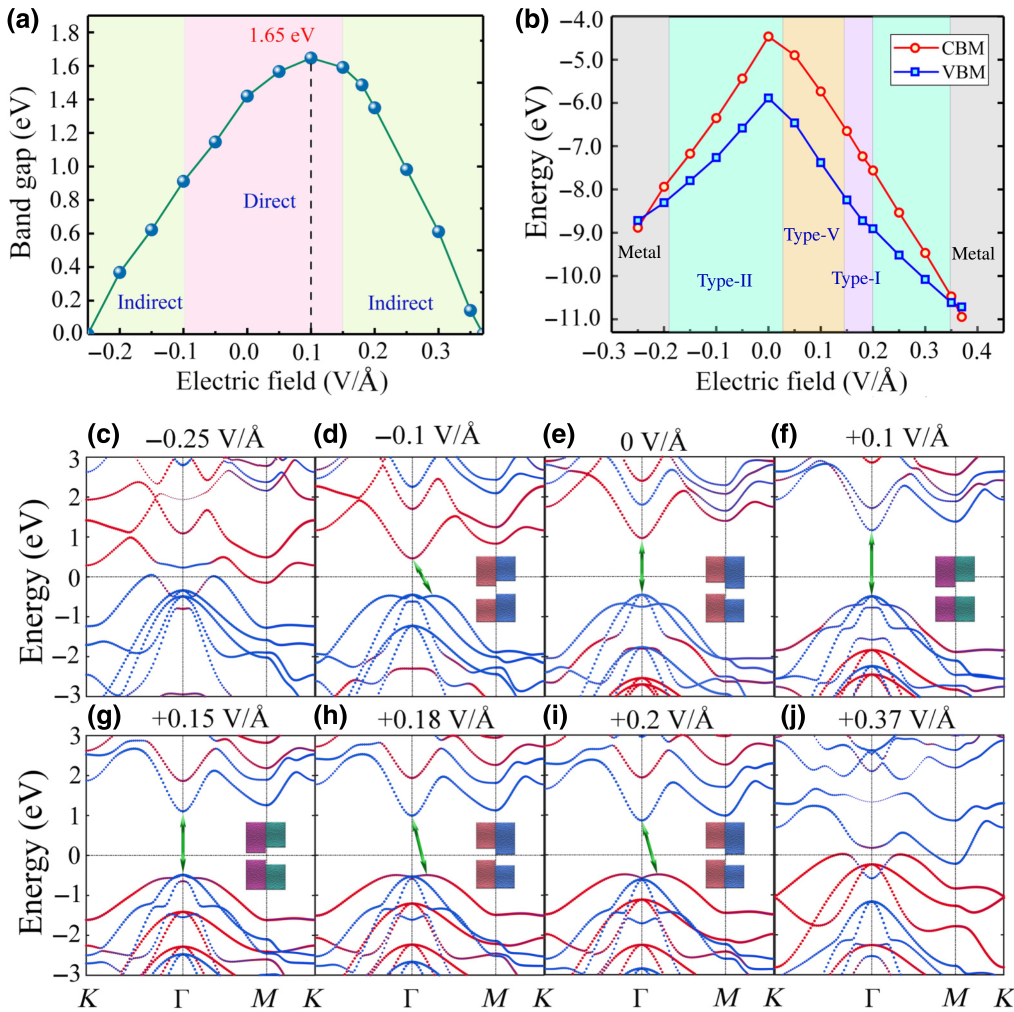

FIG. 9. (a) and (b) Evolution diagram of the band gap and the band-edge position of *AB*1 stacking with different electric fields calculated by the HSE06 functional. The projected electronic band structures of *AB*1 stacking for (c) and (d) negative and (e)–(j) positive electric field. The red and blue lines represent the InS and Janus Ga_2SeTe layers, respectively. Note that the green arrows denote the band gap of the heterostructure. The Fermi levels are shown as a black dashed lines in the figures. The schematic diagrams of the corresponding band alignments are inset in the figures.

band-edge position with external electric field is also displayed in Fig. 9(b). For the vertical direction, when the electric field is applied to the bilayer, the CBM and VBM move upward and downward as the electric field intensity increases, resulting in the monotonically decreasing trend of the band gap. Interestingly, we note that different band alignment features appear in the heterostructure. As presented in Figs. 9(c)–9(j), several specific diagrams are chosen to further describe the effects of vertical electric fields on the band structures of *AB*1 stacking. We can see the band edges of the InS monolayer gradually move upward and pass that of the Ga_2SeTe monolayer in the range of −0.1 to 0.2 V/Å of the electric field, in which the type-II, type-V, and type-I band alignment features sequentially appear in the heterostructure. Furthermore, when the intensity of the positive (negative) electric field increases to over −0.1 (0.18) V/Å, the position of the quartic band shifts up and the top of the parabolic band becomes the VBM, while the CBM is still extended on the $SeGa_2Te$ and InS monolayers, leading to the transition of direct-to-indirect band gap in the heterostructure. Based on this analysis, we can conclude that the energy levels of the Janus Ga_2SeTe/InS vdW heterostructure can be effectively modulated by increasing the amplitude of the external electric field in the vertical direction, and the diminishing band gap is induced by the corresponding movement of the CBM and VBM of the heterostructure. This illustrates that the optoelectronic devices based on the Janus Ga_2SeTe/InS vdW heterostructure can improve performance through external regulating models.

To explore the feasibility in redox reactions for water splitting under solar energy radiation, the band alignments of the InS and Ga_2SeTe monolayers, and their *AB*-stacking heterostructures are calculated using the HSE06 functional. In general, the essential criteria in full water splitting for applications in photocatalysis are that the band-edge potentials straddle the water redox potentials while the band gap is larger than the free energy of 1.23 eV. Precisely, the CB edges of materials have a higher position than the standard level for H^+/H_2 (the reduction potential of −4.44 eV), and the VB edges are lower than for O_2/H_2O (the oxidation potential of −5.67 eV) at pH = 0 (standard conditions of aqueous acid for redox reaction).

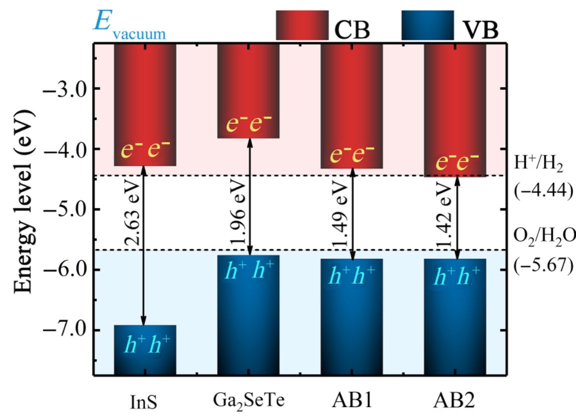

FIG. 10. Schematics of band alignment for the monolayered Janus Ga_2SeTe, InS, and corresponding vdW heterostructures (*AB*1 and *AB*2 stackings) with respect to the standard potential of oxidation (O_2/H_2O) and reduction (H^+/H_2) for water splitting. The numbers show the band gaps calculated by the HSE06 functional.

The calculated band alignments for the type-II Janus Ga_2SeTe/InS vdW heterostructures and their monolayers are depicted in Fig. 10. In two individual monolayers, the energy level position of the CBM is more positive than the reduction potential, while the VBM spans the oxidation potential, which suggests the hydrogen evolution reduction and oxygen evolution reactions can occur at the same surface simultaneously, thus resulting in the higher recombination rate of the photogenerated electron-hole pairs. Fortunately, the drawbacks can be improved on in the staggered type-II interface, where the redox reaction can take place on different individual monolayers in the heterostructure. In addition, the photocatalytic activity of Janus-based heterostructures is associated with the specific order of outermost atoms in the Janus monolayer, and similar results have been verified for GeC-*M*SSe ($M = $ Mo, W) [43]. Here, the *AB*1 stacking system ($TeGa_2Se$/InS) meets the criteria for full water splitting, showing the catalytic ability to resolve water into H^+/H_2 and O_2/H_2O. In contrast, the CBM in the *AB*2 stacking system is more positive than the reduction potential, which illustrates that it is incapable of resolving water into H^+/H_2. Thus, the *AB*1 stacking heterostructure can be regarded as a potential photocatalytic candidate material for applications in the production of clean energy.

IV. SUMMARY

In summary, we investigate the dipole effect on the electronic and optical properties of Janus Ga_2SeTe/InS heterostructures to unveil their potential for use in highly efficient solar cells by using first-principles calculations. The results show that the interface dipole appears due to the charge transfer at the interface of Janus Ga_2SeTe/InS heterostructures, and different stackings lead to different strengths of interface dipole. Meanwhile, we also find the intrinsic dipole of the Ga_2SeTe monolayer makes a significant contribution to the PCE of Janus-based heterostructures through dipole engineering. The proposed dipole engineering is based on the synergetic effect of the intrinsic dipole in 2D Janus materials and the interface dipole caused by charge transfer at the interface of 2D vdW heterostructures, which is in stark contrast to those previously used, such as applying strain or electric field. Taking the Janus Ga_2SeTe/InS heterostructure as an example, we demonstrate that the PCE can be promoted to a peak value of 23.2% when the intrinsic and interface dipoles are in the same direction, and accompanied by an appropriate applied compression strain. In addition, the Janus heterostructure possesses suitable band-edge positions of redox reaction potentials for full water splitting. Our work may herald an intrinsic yet effective way for enhancing the performance of optoelectronic devices, in contrast to the conventional external stimuli strategy.

ACKNOWLEDGMENTS

This work was supported by the National Natural Science Foundation of China (Grants No. 51772085 and No. 52172088) and Natural Science Foundation of Hunan Province (Grant No. 2020JJ4190).

[1] H. P. Zhou, Q. Chen, G. Li, S. Luo, T. B. Song, H. S. Duan, Z. R. Hong, J. B. You, Y. S. Liu, and Y. Yang, Interface engineering of highly efficient perovskite solar cells, Science **345**, 542 (2014).

[2] Y. Cui, H. F. Yao, J. Q. Zhang, K. H. Xian, T. Zhang, L. Hong, Y. M. Wang, Y. Xu, K. Q. Ma, C. B. An, C. He, Z. X. Wei, F. Gao, and J. H. Hou, Single-junction organic photovoltaic cells with approaching 18% efficiency, Adv. Mater. **32**, 1908205 (2020).

[3] Y. Cui, H. F. Yao, L. Hong, T. Zhang, Y. B. Tang, B. J. Lin, K. H. Xian, B. W. Gao, C. B. An, P. Q. Bi, W. Ma, and J. H. Hou, Organic photovoltaic cell with 17% efficiency and superior processability, Natl. Sci. Rev. **7**, 1239 (2020).

[4] Z. Yu and L. C. Sun, Recent progress on hole-transporting materials for emerging organometal halide perovskite solar cells, Adv. Energy Mater. **5**, 1500213 (2015).

[5] Y. S. Chen, P. Ye, Z. G. Zhu, X. L. Wang, L. Yang, X. Z. Xu, X. X. Wu, T. Dong, H. Zhang, J. H. Hou, F. Liu, and H. Huang, Achieving high-performance ternary organic solar cells through tuning acceptor alloy, Adv. Energy Mater. **29**, 1603154 (2017).

[6] G. Dennler, M. C. Scharber, T. Ameri, P. Denk, K. Forberich, C. Waldauf, and C. J. Brabec, Design rules for donors in bulk-heterojunction tandem solar cells-towards 15% energy-conversion efficiency, Adv. Energy Mater. **20**, 579 (2008).

[7] S. Bhattacharya, I. Baydoun, M. Lin, and S. John, Towards 30% Power Conversion Efficiency in Thin-Silicon

Photonic-Crystal Solar Cells, Phys. Rev. Appl. **11**, 014005 (2019).
[8] S. Bhattacharya and S. John, Designing High-Efficiency Thin Silicon Solar Cells Using Parabolic-Pore Photonic Crystals, Phys. Rev. Appl. **9**, 044009 (2018).
[9] S. S. Lin, Y. H. Lu, J. Xu, S. R. Feng, and J. F. Li, High performance graphene/semiconductor van der Waals heterostructure optoelectronic devices, Nano Energy **40**, 122 (2017).
[10] Y. F. Yu, S. Hu, L. Q. Su, L. J. Huang, Y. Liu, Z. H. Jin, A. A. Purezky, D. B. Geohegan, K. W. Kim, Y. Zhang, and L. Y. Cao, Equally efficient inter layer exciton relaxation and improved absorption in epitaxial and nonepitaxial MoS_2/WS_2 heterostructures, Nano Lett. **15**, 486 (2015).
[11] X. M. Li, L. Tao, Z. F. Chen, H. Fang, X. S. Li, X. R. Wang, J. B. Xu, and H. W. Zhu, Graphene and related two-dimensional materials: Structure-property relationships for electronics and optoelectronics, Appl. Phys. Rev. **4**, 021306 (2017).
[12] S. S. Lin, Z. Q. Wu, X. Q. Li, Y. J. Zhang, S. J. Zhang, P. Wang, R. Panneerselvam, and J. F. Li, Stable 16.2% efficient surface plasmon-enhanced graphene/GaAs heterostructure solar cell, Adv. Energy Mater. **6**, 1600822 (2016).
[13] B. Zhou, S. J. Gong, K. Jiang, L. P. Xu, L. Y. Shang, J. Z. Zhang, Z. G. Hu, and J. H. Chu, A type-II GaSe/GeS heterobilayer with strain enhanced photovoltaic properties and external electric field effects, J. Mater. Chem. C **8**, 89 (2020).
[14] W. Z. Dou, A. P. Huang, Y. H. Ji, X. D. Yang, Y. B. Xin, H. L. Shi, M. Wang, Z. S. Xiao, M. Zhou, and P. K. Chu, Strain-enhanced power conversion efficiency of a BP/SnSe van der Waals heterostructure, Phys. Chem. Chem. Phys. **22**, 14787 (2020).
[15] Y. Luo, S. Wang, H. Shu, J.-P. Chou, K. Ren, J. Yu, and M. Sun, A MoSSe/blue phosphorene vdw heterostructure with energy conversion efficiency of 19.9% for photocatalytic water splitting, Semicond. Sci. Technol. **35**, 125008 (2020).
[16] K. Lai, H. X. Li, Y. K. Xu, W. B. Zhang, and J. Dai, Achieving a direct band gap and high power conversion efficiency in an SbI_3/BiI_3 type-II vdW heterostructure via interlayer compression and electric field application, Phys. Chem. Chem. Phys. **21**, 2619 (2019).
[17] H. Q. Zhou, Y. Zhang, C. K. Mai, S. D. Collins, T. Q. Nguyen, G. C. Bazan, and A. J. Heeger, Conductive conjugated polyelectrolyte as hole-transporting layer for organic bulk heterojunction solar cells, Adv. Mater. **26**, 780 (2014).
[18] A. V. Krukau, O. A. Vydrov, A. F. Izmaylov, and G. E. Scuseria, Influence of the exchange screening parameter on the performance of screened hybrid functionals, J. Chem. Phys. **125**, 224106 (2006).
[19] J. Paier, M. Marsman, K. Hummer, G. Kresse, I. C. Gerber, and J. G. Angyan, Screened hybrid density functionals applied to solids, J. Chem. Phys. **124**, 154709 (2006).
[20] H. D. Bui, H. R. Jappor, and N. N. Hieu, Tunable optical and electronic properties of Janus monolayers Ga_2SSe, Ga_2STe, and Ga_2SeTe as promising candidates for ultraviolet photodetectors applications, Superlattices Microstruct. **125**, 1 (2019).
[21] L. Hu and D. S. Wei, Janus group-III chalcogenide monolayers and derivative type-II heterojunctions as water-splitting photocatalysts with strong visible-light absorbance, J. Phys. Chem. C **122**, 27795 (2018).
[22] A. Rawat, R. A. Dimple, N. Jena, M. K. Mohanta, and A. De Sarkar, Solar energy harvesting in type II van der Waals heterostructures of semiconducting group III monochalcogenide monolayers, J. Phys. Chem. C **123**, 12666 (2019).
[23] F. Ersan and C. J. P. R. A. Ataca, Janus PtX_nY_{2n} (X, Y = S, Se, Te ; $0 \leq n \leq 2$) Monolayers for Enhanced Photocatalytic Water Splitting, Phys. Rev. Appl. **13**, 064008 (2020).
[24] A. J. L. Hofmann, S. Zufle, K. Shimizu, M. Schmid, V. Wessels, L. Jager, S. Altazin, K. Ikegami, M. R. Khan, D. Neher, H. Ishii, B. Ruhstaller, and W. Brutting, Dipolar Doping of Organic Semiconductors to Enhance Carrier Injection, Phys. Rev. Appl. **12**, 064052 (2019).
[25] Hafner Kresse, Ab initio molecular-dynamics simulation of the liquid-metal-amorphous-semiconductor transition in germanium, Phys. Rev. B **49**, 14251 (1994).
[26] Furthmuller Kresse, Efficient iterative schemes for ab initio total-energy calculations using a plane-wave basis set, Phys. Rev. B **54**, 11169 (1996).
[27] S. Grimme, S. Ehrlich, and L. Goerigk, Effect of the damping function in dispersion corrected density functional theory, J. Comput. Chem. **32**, 1456 (2011).
[28] J. P. Perdew, K. Burke, and M. Ernzerhof, Generalized Gradient Approximation Made Simple, Phys. Rev. Lett. **77**, 3865 (1996).
[29] Bird White, Implementation of gradient-corrected exchange-correlation potentials in Car-Parrinello total-energy calculations, Phys. Rev. B **50**, 4954 (1994).
[30] T. Bucko, J. Hafner, S. Lebegue, and J. G. Angyan, Improved description of the structure of molecular and layered crystals: Ab initio DFT calculations with van der Waals corrections, J. Phys. Chem. A **114**, 11814 (2010).
[31] S. Grimme, Semiempirical GGA-type density functional constructed with a long-range dispersion correction, J. Comput. Chem. **27**, 1787 (2006).
[32] S. Froyen, Brillouin-zone integration by Fourier quadrature: Special points for superlattice and supercell calculations, Phys. Rev. B **39**, 3168 (1989).
[33] M. C. Scharber, D. Wuhlbacher, M. Koppe, P. Denk, C. Waldauf, A. J. Heeger, and C. L. Brabec, Design rules for donors in bulk-heterojunction solar cells - towards 10% energy-conversion efficiency, Adv. Mater. **18**, 789 (2006).
[34] Y. Guo, S. Zhou, Y. Z. Bai, and J. J. Zhao, Enhanced piezoelectric effect in Janus group-III chalcogenide monolayers, Appl. Phys. Lett. **110**, 163102 (2017).
[35] H. Z. Sun, Z. Wang, and Y. Wang, Band alignment of two-dimensional metal monochalcogenides MXs (M = Ga, In; X − S, Se, Te), Aip Adv. **7**, 095120 (2017).
[36] J. H. Chen, X. J. He, B. S. Sa, J. Zhou, C. Xu, C. L. Wen, and Z. M. Sun, III-VI van der Waals heterostructures for sustainable energy related applications, Nanoscale **11**, 6431 (2019).
[37] J. Wang, H. Guo, J. J. Xue, D. J. Chen, G. F. Yang, B. Liu, H. Lu, R. Zhang, and Y. D. Zheng, Janus Ga_2SeTe:

A promising candidate for highly efficient solar cells, Sol. RRL **3**, 1900321 (2019).

[38] Y. Si, H. Y. Wu, J. C. Lian, W. Q. Huang, W. Y. Hu, and G. F. Huang, A design rule for two-dimensional van der Waals heterostructures with unconventional band alignments, Phys. Chem. Chem. Phys. **22**, 3037 (2020).

[39] J. B. Zhao, Y. K. Li, G. F. Yang, K. Jiang, H. R. Lin, H. Ade, W. Ma, and H. Yan, Efficient organic solar cells processed from hydrocarbon solvents, Nat. Energy **1**, 15027 (2016).

[40] H. Y. Wu, K. Yang, Y. Si, W. Q. Huang, W. Y. Hu, and G. F. Huang, Two-Dimensional GaX/SnS_2 (X = S, Se) van der Waals heterostructures for photovoltaic application: Heteroatom doping strategy to boost power conversion efficiency, Phys. Status Solidi. Rapid Res. Lett. **13**, 1800565 (2019).

[41] X. Q. Li, W. C. Chen, S. J. Zhang, Z. Q. Wu, P. Wang, Z. J. Xu, H. S. Chen, W. Y. Yin, H. K. Zhong, and S. S. Lin, 18.5% efficient graphene/GaAs van der Waals heterostructure solar cell, Nano Energy **16**, 310 (2015).

[42] P. Wang, X. Q. Li, Z. J. Xu, Z. Q. Wu, S. J. Zhang, W. L. Xu, H. K. Zhong, H. S. Chen, E. P. Li, J. K. Luo, Q. K. Yu, and S. S. Lin, Tunable graphene/indium phosphide heterostructure solar cells, Nano Energy **13**, 509 (2015).

[43] H. U. Din, M. Idrees, A. Albar, M. Shafiq, I. Ahmad, C. V. Nguyen, and B. Amin, Rashba spin splitting and photocatalytic properties of GeC-MSSe (M = Mo, W) van der Waals heterostructures, Phys. Rev. B **100**, 165425 (2019).